Journal of Physics: Condensed Matter

PAPER

Pentagonal B_2N_3-based 3D metallic boron nitride with high energy density

To cite this article: Yiheng Shen *et al* 2021 *J. Phys.: Condens. Matter* **33** 165702

IOP Publishing Journal of Physics: Condensed Matter
J. Phys.: Condens. Matter **33** (2021) 165702 (7pp) https://doi.org/10.1088/1361-648X/abeffb

Pentagonal B_2N_3-based 3D metallic boron nitride with high energy density

Yiheng Shen[1,2], Huanhuan Xie[2] and Qian Wang[1,2,*]

[1] Center for Applied Physics and Technology, HEDPS, Peking University, Beijing 100871, People's Republic of China
[2] School of Materials Science and Engineering, BKL-MEMD, Peking University, Beijing 100871, People's Republic of China

E-mail: qianwang2@pku.edu.cn

Received 15 December 2020, revised 6 March 2021
Accepted for publication 18 March 2021
Published 20 April 2021

Abstract

Different from conventional insulating or semiconducting boron nitride, *metallic* BN has received increasing attention in recent years as its intrinsic metallicity grants it great potential for broad applications. In this study, by assembling the experimentally synthesized pentagonal B_2N_3 units, we have proposed the first pentagon-based three-dimensional (3D) metallic boron nitride, labeled penta-B_4N_7. First-principles calculations together with molecular dynamics simulations and convex hull diagram show that penta-B_4N_7 is not only thermally, dynamically and mechanically stable, but also three dimensionally metallic. A detailed analysis of its electronic structure reveals that the intrinsic metallicity comes from the delocalized electrons in the partially occupied antibonding N–N π orbitals. Equally important, the energy density of penta-B_4N_7 is found to be 4.07 kJ g^{-1}, which is the highest among that of all the 3D boron nitrides reported so far.

Keywords: 3D metallic BN, pentagon-based structure, high energy density, electronic structure, mechanical properties, first-principles calculation

(Some figures may appear in colour only in the online journal)

1. Introduction

Both boron and nitrogen are abundant in nature with light mass and low toxicity, and they can form diverse binary compounds with different morphologies including one-dimensional (1D) BN nanotubes [1] and nanoribbons [2], two-dimensional (2D) *h*-BN sheets [3], and three-dimensional (3D) *c*-BN [4] and *w*-BN [5]. These BN allotropes exhibit different electronic and mechanical properties, and have broad applications in various fields, including photodetectors [6], memory devices [7], field emission devices [8] and dielectric layers [9]. However, almost all these compounds are semiconducting or insulating with wide band gaps. To expand the technological applications going beyond the conventional semiconductors, it is highly desirable to design and synthesize *metallic* BN compounds. Thus, a number of metallic BN structures have been predicted [10–14]. For instance, it has been found that using $B_3N_3H_6$ as the precursor of building unit, the interlocking hexagonal B_3N_3 can form a stable 3D metallic BN compound [10]. By changing B/N atomic ratios, some metallic B_xN_y compounds have also been found like *t*-B_2N_3 [11] and *t*-B_3N_4 [12], both of them possess ultrahigh Vickers hardness as they contain the hexagonal structure units of *c*-BN.

However, in all the reported 3D metallic boron nitrides, none of them are found to consist of pentagonal structure units that form many unconventional structures with novel properties, as shown in penta-graphene with negative Poisson's ratio [15], penta-silicene with ferroelectricity [16], penta-BCN with piezoelectricity [17], penta-MnN_2 with high Curie temperature ferromagnetism [18], penta-ZnS_2 with large out-of-plane second harmonic generation susceptibility [19], penta-$PdSe_2$ with photocatalyticity [20] and thermoelectricity [21], penta-CN_2 with exceptionally high lattice thermal conductivity [22], 3D penta-C with ultra-high ideal strength [23], penta-RuS_4

* Author to whom any correspondence should be addressed.

with quantum topological phase [24], etc. More details can be found in our database for pentagon-based sheets [25]. It is also encouraging to note that some pentagonal B_2N_3 radicals were synthesized [26] that can be used as the structural units for the design of 3D pentagon-based boron nitrides. These advances in using pentagons for designing new materials motivate us to carry out this study. As demonstrated below, a B_2N_3-based 3D pentagonal structure, penta-B_4N_7, is constructed, which exhibits robust stability, metallicity and high energy density.

2. Computational methods

All first-principles calculations are performed within the scheme of density functional theory by using the Vienna *ab initio* simulation package [27, 28], where the exchange–correlation term is treated by using the generalized gradient approximation [29] with the Perdew–Burke–Ernzerhof (PBE) functional [30] in geometry optimization and properties calculations, and the Heyd–Scuseria–Ernzerhof (HSE06) hybrid functional [31, 32] in electronic structure calculations. The electron–ion interaction is described by the projected augmented wave method [33]. The plane waves with a kinetic energy cutoff of 600 eV are used to expand the wavefunctions. The k-points for integration in the first Brillouin zone are sampled by using a $9 \times 9 \times 9$ grid for geometry optimization and properties calculations, and a $15 \times 15 \times 15$ grid for electronic structure calculations. The convergence thresholds of the total energy and the total force on each atom are set to 10^{-8} eV and 10^{-6} eV·Å^{-1}, respectively. The phonon band structure is calculated by using the finite displacement method as implemented in Phonopy [34]. *Ab initio* molecular dynamic (AIMD) simulations under canonical (NVT) ensemble are carried out with Nosé–Hoover thermostat [35].

3. Results and discussion

3.1. Geometry and stability

The design of new pentagon-based structures has been challenging for ages due to the forbidden five-fold rotational symmetry in the crystal structures. Here, we take a short cut to bypass such inconvenience by using the synthesized radical [26] (figure 1(a)) as the precursor of pentagonal B_2N_3 unit to assemble a pentagon-based structural motif via bond sharing, namely, sharing each B–N bond of the B_2N_3 unit with its neighboring three units. Thus, a pentagon-based structural motif B_4N_{13} with T_d symmetry is formed, as shown in figure 1(b), which features the concurrent three-fold rotation and four-fold rotatory inversion axes, providing the possibility of forming a cubic lattice. The motifs are periodically arranged by sharing the six N–N bonds in each motif with its six neighboring motifs, naturally forming a B_2N_3-based 3D crystal structure with a cubic lattice, containing a total of 32 B atoms and 56 N atoms, and leading to an atomic ratio of B to N of 4:7. Thus, we name this structure penta-B_4N_7.

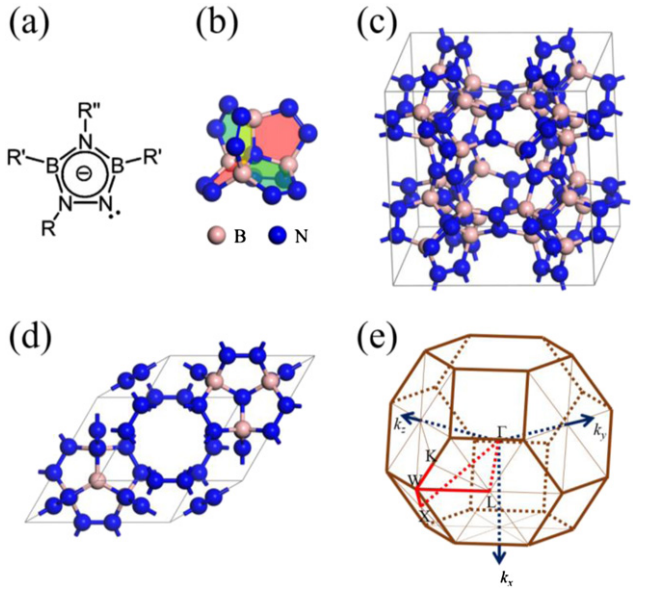

Figure 1. (a) Precursor of the B_2N_3 unit. (b) Structural motif, (c) unit cell, (d) primitive cell, and (e) high symmetry path W(0.5, 0.25, 0.75)-L(0.5, 0.5, 0.5)-Γ(0, 0, 0)-X(0.5, 0, 0.5)-W–K(0.375, 0.375, 0.375) (red lines) in the first Brillouin zone of penta-B_4N_7.

The optimized geometry of the B_2N_3-based penta-B_4N_7 is shown in figure 1(c), which has a cubic unit cell with the $Fm-3m$ symmetry (space group no. 225) and the lattice parameters of $a = b = c = 9.27$ Å, $\alpha = \beta = \gamma = 90°$. The optimized atomic coordinates of B atoms in the unit cell occupy the Wyckoff position 32f (0.1547, 0.1547, 0.1547), and those of N atoms occupy the Wyckoff positions 8c (0.25, 0.25, 0.25) and 48h (0.0, 0.3018, 0.3018). The coordination of these atoms in penta-B_4N_7 inherits that in the structural motif, where the tetrahedral four-fold coordinated N atoms at the 8c position are saturated by the identically coordinated B atoms at the 32f position, and the B atoms are further saturated by the N atoms at the 48h position. To affirm the hybridization of these atoms, the bond lengths in this structure are evaluated, where the B–N bond lengths of 1.53–1.54 Å are comparable to that in c-BN, while the N–N bond length of 1.36 Å falls in between that in hydrazine (NH_2–NH_2, 1.46 Å) [36] and diimide (NH = NH, 1.25 Å) [37], indicating its weak double bond-like nature. These bond parameters suggest that the penta-B_4N_7 lattice is constructed by three types of atoms, namely sp^3-hybridized N, sp^3-hybridized B, and sp^2-hybridized N atoms.

We first examine the phase stability of penta-B_4N_7. The formation enthalpy ΔH of this structure and other B_xN_y compounds is defined as:

$$\Delta H = H(B_xN_y) - \left[\frac{x}{x+y} \cdot H(B) + \frac{y}{x+y} \cdot H(N)\right], \quad (1)$$

here $H(B_xN_y)$, $H(B)$ and $H(N)$ are the enthalpies of the B_xN_y structure and the α-Boron and α-N_2 phase, respectively, normalized on a per-atom basis. The results are summarized in the convex hull diagram in figure 2(a), where h-BN ($x = 0.5$, $\Delta H = -1.31$ eV atom^{-1}) together with the elemental

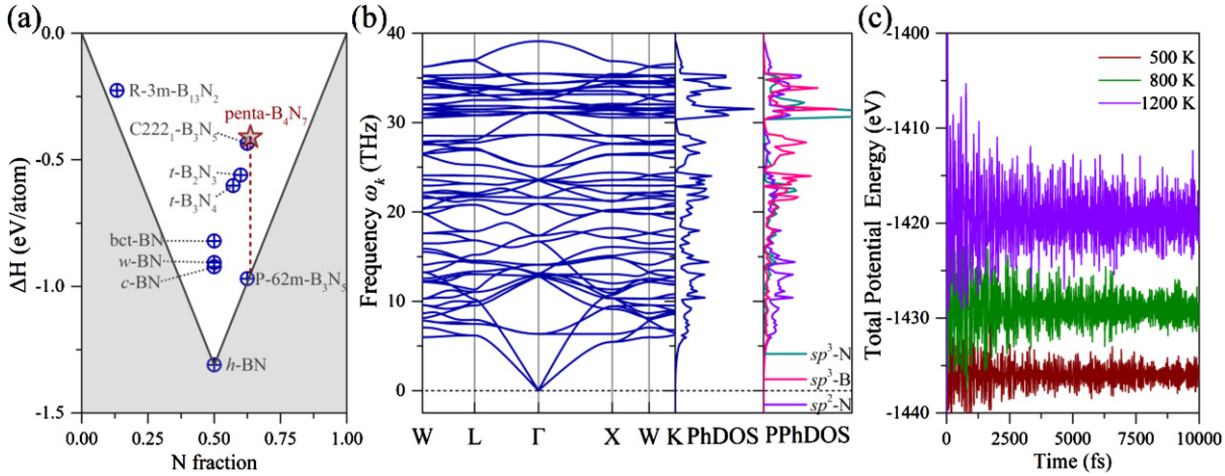

Figure 2. (a) Convex hull diagram of the B_xN_y system. (b) Phonon spectrum, PhDOS and PPhDOS of penta-B_4N_7. (c) Energy fluctuation of penta-B_4N_7 during AIMD simulations at the different temperatures.

B ($x = 0$, $\Delta H = 0$) and N ($x = 1$, $\Delta H = 0$) are the thermodynamically stable structures in the B_xN_y system. The formation enthalpy of penta-B_4N_7 is -0.41 eV atom^{-1}, indicating that this structure is relatively stable with respect to elemental B and N. However, its enthalpy is 0.54 eV atom^{-1} above the tie line between *h*-BN and N_2, as illustrated by the dashed line in figure 2(a). The energy density Q_e of this structure is defined as

$$Q_e = H(B_4N_7) - \left[\frac{8}{11}\cdot H(\mathrm{BN}) + \frac{3}{11}\cdot H(\mathrm{N})\right], \qquad (2)$$

where $H(B_4N_7)$ and H(BN) are the enthalpies per atom of penta-B_4N_7 and *h*-BN, respectively. As a result, penta-B_4N_7 is thermodynamically metastable, and the dissociation from penta-B_4N_7 to *h*-BN and N_2 is highly exothermic with an energy density of 4.07 kJ g^{-1}, higher than that of any previously reported B_xN_y compounds like *t*-B_2N_3 and $C222_1$-B_3N_5, as shown in table 1, which makes penta-B_4N_7 a potential high energy density material (HEDM) [38]. The high energy density of this structure can be attributed to its N rich feature together with its double bond-like N–N bonds [39–41]. While it is difficult to synthesize materials with such a high energy density in ambient environment, the synthesis can be possible at high pressure with low-nitrogen precursors and N_2 [42, 43], where the change of the $p{\cdot}V$ term in the Gibbs free energy would result in the inversion of ground state structure between solid state nitrogen-rich compound and compressed N_2. Meanwhile, the high energy density of penta-B_4N_7 does not necessarily leads to its instability at ambient conditions, because the stability can still be guaranteed by a deep enough potential well in the configuration space of BN compounds.

Thus, we then check the dynamical stability of penta-B_4N_7 by calculating its phonon band structure. The primitive cell and the corresponding high symmetry path in its first Brillouin zone, as shown in figures 1(d) and (e) respectively, are used for the calculation. The resulting phonon band structure and phonon density of states (PhDOS) are presented in figure 2(b), which shows that there is no any imaginary phonon modes in the entire first Brillouin zone, indicating that penta-B_4N_7 is dynamically stable. The phonon group velocity $v_g = \partial\omega_k/\partial k$ of the longitudinal acoustic and the two transverse acoustic branches is 12.4 and 8.17 km s^{-1}, respectively. The low-lying optical modes below 15.0 THz overlap with the acoustic modes, and are mainly contributed by the sp^2-hybridized N atoms according to the partial PhDOS (PPhDOS) in figure 2(b), due to the vibration of N_2 dimer in the lattice. While the high-frequency optical modes above 30 THz are contributed by the coupling among the different types of atoms.

We also examine the thermal stability of penta-B_4N_7 by performing AIMD simulations at different temperatures, i.e. 500, 800 and 1200 K, respectively, for 10 ps with a time step of 1 fs. A $2 \times 2 \times 2$ supercell of the penta-B_4N_7 primitive cell is used

Table 1. Energy density Q_e (in kJ g^{-1}), Young's modulus E (in GPa), Poisson's ratio ν, Vickers hardness H_v (in GPa) and energy band gap Δ_{gap} (in eV) calculated at the HSE06 level of penta-B_4N_7. The corresponding properties of several B–N compounds are also given for comparison.

Structure	Q_e	E	ν	H_v	Δ_{gap}	Ref
Penta-B_4N_7	4.07	418.7	0.19	28.4	0	
t-B_2N_3	2.95	695	0.16	53	0[a]	[11]
t-B_3N_4	—	676.6[b]	0.17[b]	42.8	0	[12]
c-B_3N_4	—	580.5	0.191	34.2	—	[44]
c-B_3N_4	—	569.9	0.195	33.0	—	[d]
Pm–3*n*-BN	—	—	—	58.4[c]	5.9	[45]
$C222_1$-B_3N_5	3.44	—	—	78.5[c]	0.775	[45]
M-BN	—	583.9[b]	0.19[b]	35.4	0	[13]
c-BN	—	718[b]	0.18[b]	65[c]	6.4	[45]
c-BN	—	722.6	0.182	44.3	—	[d]
h-BN	—	—	—	—	5.2	[45]
P-BN	—	846	0.15[b]	60.5	5.51[a]	[46]
Cubic-B_6N_6	—	675.8	0.09	—	5.97	[47]
Cubic-B_6N_6	—	683.5	0.11	—	—	[d]

[a]Calculated at the PBE level.
[b]Deduced from raw data in corresponding literature.
[c]Evaluated using a different empirical model proposed by Gao *et al* in reference [48].
[d]Our calculated results.

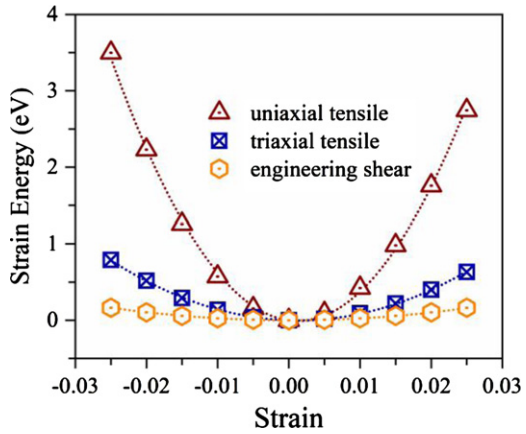

Figure 3. Variation of the strain energy with uniaxial and triaxial tensile strain, and the engineering shear strain, respectively, for penta-B_4N_7.

in the simulations to avoid the fake instability caused by the periodic boundary condition. The variations of the total potential energies with simulation time for the different temperatures are plotted in figure 2(c), which shows the fluctuations of the total potential energies around the constant values. In addition, we find that the geometry of penta-B_4N_7 remains almost unchanged at the end of these simulations. Therefore, we conclude that penta-B_4N_7 is thermally stable, and can withstand high temperature up to 1200 K.

3.2. Mechanical properties

Next, we evaluate the mechanical properties of penta-B_4N_7. Due to the symmetry constraints of the cubic lattice, the stiffness tensor **C** of penta-B_4N_7 has only three nonzero independent components, namely C_{11} ($=C_{22} = C_{33}$), C_{12} ($=C_{13} = C_{23}$) and C_{44} ($=C_{55} = C_{66}$) under Voigt notation [49]. The tensor components are obtained by the parabolic fitting of the energy–strain relationship based on the equations: $E_{\mathrm{uni}} = C_{11}\cdot\varepsilon^2/2$, $E_{\mathrm{tri}} = (3C_{11}/2 + 3C_{12}) \cdot \varepsilon^2$, and $E_{\mathrm{shear}} = C_{44}\cdot\gamma_{\mathrm{t}}{}^2/2 = C_{44}\cdot\gamma_{\mathrm{e}}{}^2/8$, respectively, here E is strain energy, ε is tensile strain, and γ_{e} is engineering shear strain, which equals twice the tensor shear strain γ_{t}. To calculate the strain energy of penta-B_4N_7, we force a gradient of the uniaxial/triaxial tensile strain ε and the engineering shear strain γ_{e} on the shape of the penta-B_4N_7 unit cell, and optimize the geometry with fixed lattice parameters to mimic their effect on the lattice. As shown in figure 3, the resulting C_{11}, C_{12} and C_{44} are 458.0, 105.2 and 88.9 GPa, respectively, which satisfy the Born–Huang criteria ($C_{11} > C_{12}$, $C_{11} + 2C_{12} > 0$ and $C_{44} > 0$), and thus demonstrate the mechanical stability of penta-B_4N_7.

We then calculate the mechanical properties of penta-B_4N_7 from the stiffness tensor **C**. The Young's modulus E is obtained using the following equation [50]:

$$E = [s_{11} - (2s_{11} - 2s_{12} - s_{44}) \times (\cos^2\theta\sin^2\theta + \sin^4\theta\cos^2\varphi\sin^2\varphi)]^{-1}, \quad (3)$$

here θ and φ are the Euler's angles, and $(s_{ij})_{6\times6} = (C_{ij})^{-1}_{6\times6}$. The shear modulus G and Poisson's ratio ν are then calculated

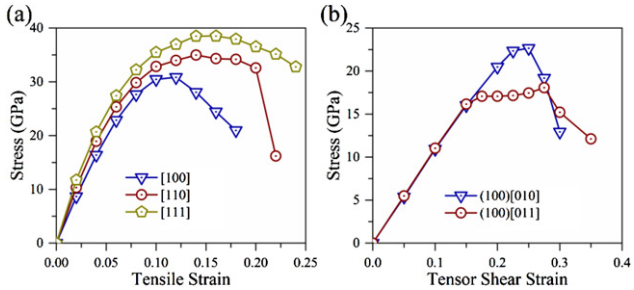

Figure 4. Stress–strain relationship of the typical (a) tensile and (b) tensor shear strain in penta-B_4N_7.

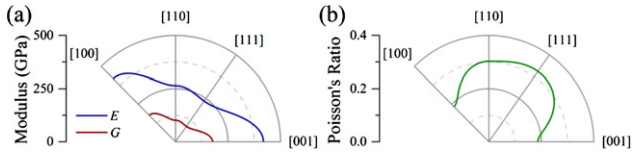

Figure 5. (a) Young's modulus E, shear modulus G, and (b) Poisson's ratio of penta-B_4N_7 with respect to crystalline directions.

from the Young's modulus E and bulk modulus $B = (C_{11} + 2C_{12})/3 = 222.8$ GPa based on the equation: $2G\cdot(1 + \nu) = E = 3B\cdot(1 - 2\nu)$. The Vickers hardness H_{v} is further deduced from these parameters using the empirical model [51], $H_{\mathrm{v}} = 2(k^2G)^{0.585} - 3$, here $k = G/B$ is the Pugh's ratio.

The calculated Young's modulus, shear modulus and Poisson's ratio along the axial directions read $E_0 = 418.7$ GPa, $G_0 = 176.4$ GPa, and $\nu_0 = 0.19$, respectively, and the resulting H_{v} is 28.4 GPa. For comparison, these mechanical properties of other B_xN_y compounds are also listed in table 1. The axial Young's modulus of penta-B_4N_7 is only about 2/3 of that of c-BN, and is smaller than that of other previously reported B_xN_y compounds, and its Vickers hardness shows an identical trend, indicating that the bonds in penta-B_4N_7 are weaker than those of the fellow B_xN_y compounds [52]. Notably, the H_{v} of penta-B_4N_7 is much lower than that of the HEDMs t-B_2N_3 (53 GPa) [11] and $C222_1$-B_3N_5 (78.5 GPa) [45]. This can be attributed to the excessive N–N bonds orientated in all three axial directions of the penta-B_4N_7 unit cell instead of those in t-B_2N_3 and $C222_1$-B_3N_5 along one axial direction. Because the model for Vickers hardness evaluates the hardness of polycrystalline materials, and as a result, a low hardness is predicted only when all axial directions are weakened. The reliability of the empirical model for Vickers hardness is confirmed by the stress–strain relationships in figure 4, where the ideal tensile and shear strength of penta-B_4N_7, defined by the minimal peak stress values on the stress–strain curves, are 30.8 GPa at the tensile strain of 0.12 along the [100] direction and 18.1 GPa at the shear strain of 0.275 along the [011] direction, respectively. The ideal strength of penta-B_4N_7, which is often regarded as an estimation of the Vickers hardness [11], is comparable to our prediction of its Vickers hardness (28.4 GPa).

The orientation-related mechanical properties of penta-B_4N_7 are plotted in figure 5, displaying significant anisotropy with the maximum and minimum of the Young's moduli E (and the shear moduli G as well) along the [100] and [111]

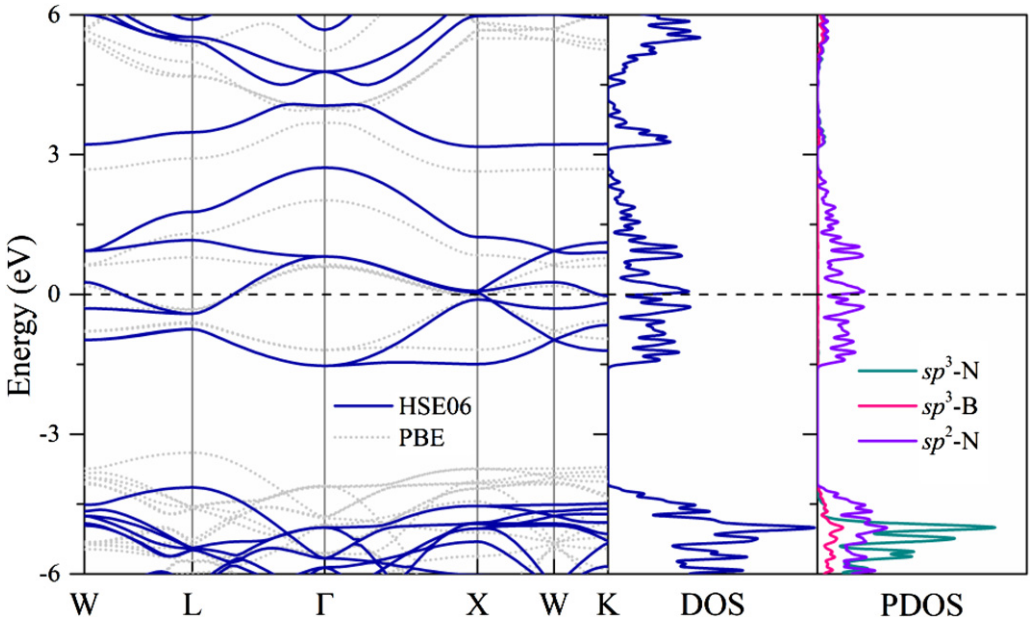

Figure 6. Electronic band structure, total DOS, and PDOS of the *p* orbitals of B and N atoms of penta-B_4N_7.

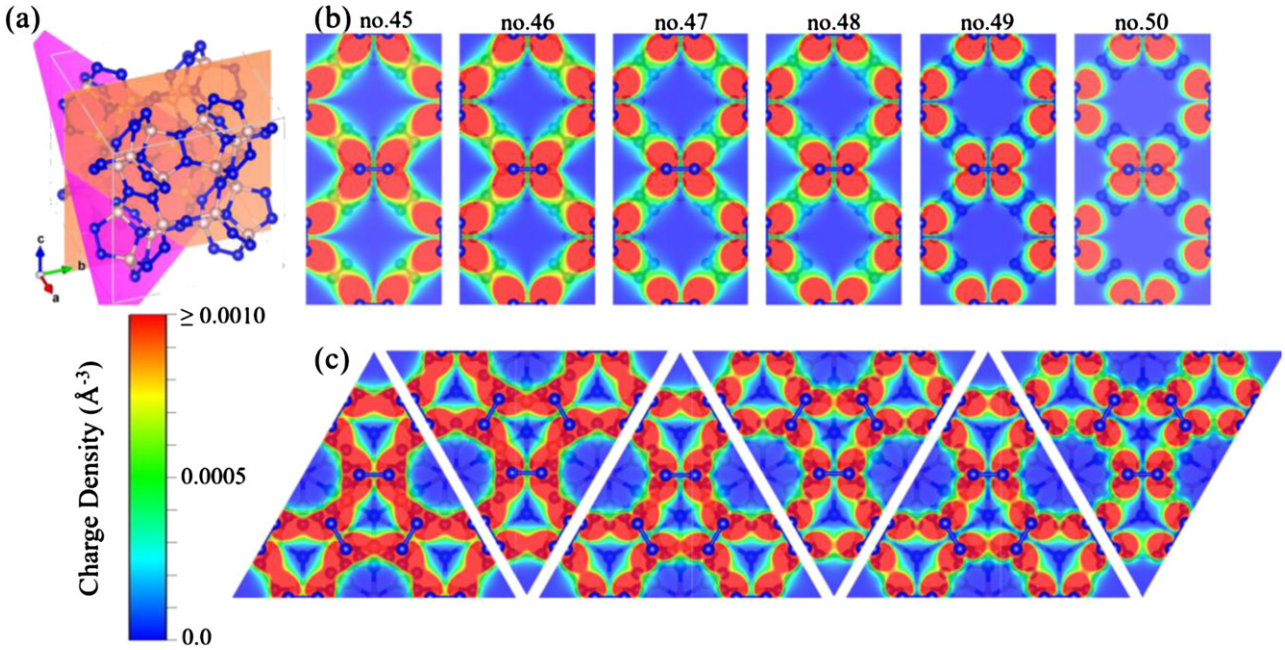

Figure 7. (a) Schematic of the (100) (in orange) and (111) (in magenta) planes of penta-B_4N_7 that contain the N–N bonds. Band-decomposed charge density of energy bands within the energy range of (−3 eV, 3 eV) on the (b) (100) and (c) (111) plane.

directions, respectively, while the Poisson's ratio ν shows an exactly reverse pattern. The maximum values in the three cases are all about twice as large as the minimum ones.

3.3. Electronic structure

Next, we calculate the electronic band structure of penta-B_4N_7 at the HSE06 level by using its primitive cell, which contains 8 B and 14 N atoms with a total of 47 pairs of valence electrons. It is worth noting that, from the perspective of the linear combination of atomic orbitals, a total of 88 atomic orbitals of the B and N atoms (one 2*s* and three 2*p* orbitals for each atom) lead to 44 bonding states and 44 antibonding states, indicating that three pairs of valence electrons in this structure will occupy antibonding states. As shown in the electronic band structure, and the total density of states (DOS) and partial DOS (PDOS) in figure 6, penta-B_4N_7 exhibits robust intrinsic metallicity with multiple energy bands crossing the Fermi level and a fairly large DOS of 3.19 eV^{-1} at the Fermi level. By analyzing the PDOS of the *p* orbitals of the sp^2- and sp^3-hybridized *N* and sp^3-hybridized B atoms, we find that the DOS of penta-B_4N_7 near the Fermi level is mostly contributed

by the p orbitals of the sp^2-hybridized N atoms, namely, the π bonds of the N_2 dimers. This feature is further confirmed by the band-decomposed charge densities on the vertical cross section of the N–N bonds (the (100) plane in figure 7(a)), where the shape of the six energy bands in the range between ±3 eV around the Fermi level (energy bands no. 45–50) are all distributed on the sp^2-hybridized N atoms with antibonding π state nature, as shown in figure 7(b). The six energy bands correspond to the linear combination of the six antibonding N–N π orbitals in each penta-B_4N_7 primitive cell, and the partial occupation of these antibonding states, more specifically, the one-electron occupation of each N–N antibonding π orbital due to the symmetry of penta-B_4N_7, weakens the N–N π bonds in the N_2 dimmers without de facto breaking it by the full occupation of the antibonding π orbitals, explaining the reason why the N–N bonds in this structure are weaker in strength and longer in length than that of typical N=N double bond, and thus contributes to the large energy density of penta-B_4N_7. Furthermore, these half-occupied antibonding N–N π orbitals are highly delocalized, so that they thoroughly overlap with their neighbors on the {111} family of crystal planes, as shown in figure 7(c). Such overlapping leads to a 3D framework of metallic channels rather than the 2D and 1D metallicities in other metallic B_xN_y compounds like t-B_2N_3 [11], t-B_3N_4 [12], and M-BN [13], because their metallic channels are all interrupted by electron-deficient B atoms in one direction or two. This property is expected because of the equivalence of the three axial directions in penta-B_4N_7 as guaranteed by its cubic symmetry, and it is supported by the electronic band structure of penta-B_4N_7, where the energy bands intersect with the Fermi level on all high symmetry paths but Γ–X. This sole exception in the momentum space corresponds to the progression of electrons along the axial directions of the penta-B_4N_7 unit cell, where the overlapping of the antibonding π orbitals is limited, as illustrated in figure 7(b).

4. Conclusions

In summary, by performing state-of-the-art first principles calculations, we have proposed a new nitrogen-rich pentagon-based 3D boron nitride, penta-B_4N_7, which is constructed by using the experimentally synthesized pentagonal B_2N_3 as its structural unit, and confirmed its thermal, dynamical and mechanical stabilities. More importantly, penta-B_4N_7 is the first pentagon-based 3D metallic boron nitride, and its intrinsic metallicity comes from the delocalized electrons in the half-occupied antibonding N–N π orbitals. In addition, the energy density of penta-B_4N_7 is found to be the highest one among that of all the 3D boron nitrides studied so far. Our study expands the boron nitride family with new features not only in geometric configuration but also in functionalities.

Acknowledgments

This work is partially supported by grants from the National Natural Science Foundation of China (Grant Nos. NSFC-21773004 and NSFC-11974028), the National Key Research and Development Program of the Ministry of Science and Technology of China (2017YFA0205003), and is supported by the High Performance Computing Platform of Peking University, China.

Data availability statement

The data that support the findings of this study are available upon reasonable request from the authors.

ORCID iDs

Huanhuan Xie https://orcid.org/0000-0002-3292-9039
Qian Wang https://orcid.org/0000-0002-9766-4617

References

[1] Golberg D, Bando Y, Huang Y, Terao T, Mitome M, Tang C and Zhi C 2010 *ACS Nano* **4** 2979–93
[2] Zeng H, Zhi C, Zhang Z, Wei X, Wang X, Guo W, Bando Y and Golberg D 2010 *Nano Lett.* **10** 5049–55
[3] Lin Y, Williams T V and Connell J W 2010 *J. Phys. Chem. Lett.* **1** 277–83
[4] Hirano S-I, Yamaguchi T and Naka S 1981 *J. Am. Ceram. Soc.* **64** 734–6
[5] Ji C, Levitas V I, Zhu H, Chaudhuri J, Marathe A and Ma Y 2012 *Proc. Natl Acad. Sci.* **109** 19108–12
[6] Zheng W, Lin R, Zhang Z and Huang F 2018 *ACS Appl. Mater. Interfaces* **10** 27116–23
[7] Wu X *et al* 2019 *Adv. Mater.* **31** 1806790
[8] Zhirnov V V, Wojak G J, Choi W B, Cuomo J J and Hren J J 1997 *J. Vac. Sci. Technol.* A **15** 1733–8
[9] Kim K K, Hsu A, Jia X, Kim S M, Shi Y, Dresselhaus M, Palacios T and Kong J 2012 *ACS Nano* **6** 8583–90
[10] Zhang S, Wang Q, Kawazoe Y and Jena P 2013 *J. Am. Chem. Soc.* **135** 18216–21
[11] Lin S *et al* 2019 *J. Mater. Chem.* C **7** 4527–32
[12] Xie C *et al* 2017 *J. Mater. Chem.* C **5** 5897–901
[13] Xiong M, Luo K, Pan Y, Liu L, Gao G, Yu D, He J, Xu B and Zhao Z 2018 *J. Alloys Compd.* **731** 364–8
[14] Dai J, Wu X, Yang J and Zeng X C 2013 *J. Phys. Chem. Lett.* **4** 3484–8
[15] Zhang S, Zhou J, Wang Q, Chen X, Kawazoe Y and Jena P 2015 *Proc. Natl Acad. Sci.* **112** 2372–7
[16] Guo Y, Zhang C, Zhou J, Wang Q and Jena P 2019 *Phys. Rev. Appl.* **11** 064063
[17] Zhao K, Guo Y, Shen Y, Wang Q, Kawazoe Y and Jena P 2020 *J. Phys. Chem. Lett.* **11** 3501–6
[18] Zhao K and Wang Q 2020 *Appl. Surf. Sci.* **505** 144620
[19] Shen Y, Guo Y and Wang Q 2020 *Adv. Theory Simul.* **3** 2000027
[20] Long C, Liang Y, Jin H, Huang B and Dai Y 2018 *ACS Appl. Energy Mater.* **2** 513–20
[21] Sun M, Chou J-P, Shi L, Gao J, Hu A, Tang W and Zhang G 2018 *ACS Omega* **3** 5971–9
[22] Wang H, Qin G, Qin Z, Li G, Wang Q and Hu M 2018 *J. Phys. Chem. Lett.* **9** 2474–83
[23] Zhu X and Su H 2017 *J. Phys. Chem.* C **121** 13810–5
[24] Yuan S, Zhou Q, Wu Q, Zhang Y, Chen Q, Hou J-M and Wang J 2017 *npj 2D Mater. Appl.* **1** 29
[25] Shen Y P and Wang Q 2020 Database for pentagon-based sheets http://pubsd.com/
[26] Ly H V, Chow J H, Parvez M, McDonald R and Roesler R 2007 *Inorg. Chem.* **46** 9303–11

[27] Kresse G and Furthmüller J 1996 *Comput. Mater. Sci.* **6** 15–50
[28] Kresse G and Furthmüller J 1996 *Phys. Rev.* B **54** 11169–86
[29] Teter M P, Payne M C and Allan D C 1989 *Phys. Rev.* B **40** 12255–63
[30] Perdew J P, Burke K and Ernzerhof M 1996 *Phys. Rev. Lett.* **77** 3865–8
[31] Heyd J, Scuseria G E and Ernzerhof M 2003 *J. Chem. Phys.* **118** 8207–15
[32] Heyd J, Scuseria G E and Ernzerhof M 2006 *J. Chem. Phys.* **124** 219906
[33] Blöchl P E 1994 *Phys. Rev.* B **50** 17953–79
[34] Togo A and Tanaka I 2015 *Scr. Mater.* **108** 1–5
[35] Nosé S 1984 *J. Chem. Phys.* **81** 511–9
[36] Collin R L and Lipscomb W N 1951 *Acta Crystallogr.* **4** 10–4
[37] Carlotti M, Johns J W C and Trombetti A 1974 *Can. J. Phys.* **52** 340–4
[38] Mailhiot C, Yang L H and McMahan A K 1992 *Phys. Rev.* B **46** 14419–35
[39] Wei S, Li D, Liu Z, Wang W, Tian F, Bao K, Duan D, Liu B and Cui T 2017 *J. Phys. Chem.* C **121** 9766–72
[40] Wei S, Li D, Liu Z, Li X, Tian F, Duan D, Liu B and Cui T 2017 *Phys. Chem. Chem. Phys.* **19** 9246–52
[41] Zhang S, Zhou J, Wang Q and Jena P 2016 *J. Phys. Chem.* C **120** 3993–8
[42] Steele B A, Stavrou E, Crowhurst J C, Zaug J M, Prakapenka V B and Oleynik I I 2017 *Chem. Mater.* **29** 735–41
[43] Bykov M *et al* 2018 *Nat. Commun.* **9** 2756
[44] Zhang B 2016 *J. Alloys Compd.* **663** 862–6
[45] Li Y, Hao J, Liu H, Lu S and Tse J S 2015 *Phys. Rev. Lett.* **115** 105502
[46] Jiang X, Zhao J and Ahuja R 2013 *J. Phys.: Condens. Matter* **25** 122204
[47] Mei H Y, Cai X H, Tang M, Hui Q, Song Q and Wang M 2019 *Comput. Mater. Sci.* **162** 111–5
[48] Gao F, He J, Wu E, Liu S, Yu D, Li D, Zhang S and Tian Y 2003 *Phys. Rev. Lett.* **91** 015502
[49] Le Page Y and Saxe P 2002 *Phys. Rev.* B **65** 104104
[50] Uesugi T, Takigawa Y and Higashi K 2005 *Mater. Trans.* **46** 1117–21
[51] Chen X-Q, Niu H, Li D and Li Y 2011 *Intermetallics* **19** 1275–81
[52] Gao F 2006 *Phys. Rev.* B **73** 132104